

LiDAR-guided Stereo Matching with a Spatial Consistency Constraint

Yongjun Zhang ^{a,*,1}, Siyuan Zou ^{a,1}, Xinyi Liu ^{a,*}, Xu Huang ^b, Yi Wan ^a, and Yongxiang Yao ^a

a School of Remote Sensing and Information Engineering, Wuhan University, Wuhan 430079, China

b School of Geospatial Engineering and Science, Sun Yat-Sen University, Zhuhai 519082, China

* Corresponding authors.

¹ Both authors contributed equally to this manuscript.

E-Mail: zhangyj@whu.edu.cn (Y. Zhang), zousiyuan3s@whu.edu.cn (S. Zou), liuxy0319@whu.edu.cn (X. Liu), huangx358@mail.sysu.edu.cn (X. Huang), yi.wan@whu.edu.cn (Y. Wan), yaoyongxiang@whu.edu.cn (Y. Yao)

Abstract: The complementary fusion of light detection and ranging (LiDAR) data and image data is a promising but challenging task for generating high-precision and high-density point clouds. This study proposes an innovative LiDAR-guided stereo matching approach called LiDAR-guided stereo matching (LGSM), which considers the spatial consistency represented by continuous disparity or depth changes in the homogeneous region of an image. The LGSM first detects the homogeneous pixels of each LiDAR projection point based on their color or intensity similarity. Next, we propose a riverbed enhancement function to optimize the cost volume of the LiDAR projection points and their homogeneous pixels to improve the matching robustness. Our formulation expands the constraint scopes of sparse LiDAR projection points with the guidance of image information to optimize the cost volume of pixels as much as possible. We applied LGSM to semi-global matching and AD-Census on both simulated and real datasets. When the percentage of LiDAR points in the simulated datasets was 0.16%, the matching accuracy of our method achieved a subpixel level, while that of the original stereo matching algorithm was 3.4 pixels. The experimental results show that LGSM is suitable for indoor, street, aerial, and satellite image datasets and provides good transferability across semi-global matching and AD-Census. Furthermore, the qualitative and quantitative evaluations demonstrate that LGSM is superior to two state-of-the-art optimizing cost volume methods, especially in reducing mismatches in difficult matching areas and refining the boundaries of objects.

Keywords: LiDAR; Stereo matching; Semi-Global Matching; AD-Census; Multi-modal data fusion; Spatial consistency constraint

1. Introduction

Three-dimensional (3D) perception is the digitization of real spatial information ([Hu et al., 2021](#); [Landeschi, 2018](#); [Moisan et al., 2021](#)), which plays an important role in the areas of cultural heritage ([Xiao et al., 2018](#)), robotic navigation ([Nefti-Meziani et al., 2015](#)), autonomous driving ([Arnold et al., 2019](#)), vegetation investigation ([Zhang and Khoshelham, 2020](#)), change detection ([Zhou et al., 2020](#)), and building extraction ([Liu et al., 2020](#)).

The automatic 3D reconstruction of objects and scenes at different scales is performed using range or image data. Active or range sensors, such as structured light scanners or laser scanners, are a common source of dense point clouds because of their convenience, speed, and ability to capture millions of points in a short time ([Remondino et al., 2014](#)). However, structured light scanners commonly fail in the presence of sunlight and provide a limited sensing range ([Salvi et al., 2004](#)), and laser scanners have difficulty obtaining high-density and large-scale point clouds when data acquisition budgets are limited ([Paris and Bruzzone, 2014](#)). Compared with light detection and ranging (LiDAR), the image-based approach is a passive, pixel-by-pixel, and low-cost technology for obtaining the 3D structure of a scene that has a higher density and finer topography. In difficult matching areas, such as shadows, low textures, and repeated textures, the image-based approach is often inaccurate, and LiDAR point clouds respond better than that in the aforementioned areas ([Maltezos et al., 2016](#)). Therefore, the complementary fusion of LiDAR data and image data is a promising solution for generating dense, accurate, and texture-rich point clouds ([Huang et al., 2018](#)).

The fusion methods of LiDAR data and image data can have different levels. The levels depend on the differences in the emphasis of the data sources, such as: 1) point cloud fusion, 2) LiDAR data interpolation aided by images, and 3) dense image matching (DIM) constrained by LiDAR data. Point cloud fusion directly integrates LiDAR data and DIM point clouds, which play an important role in geoscience applications, such as digital surface model (DSM) generation ([Schenk and Csathó, 2002](#)), urban 3D modeling ([Gao et al., 2020](#); [Mandlbürger et al., 2017](#)), and forest resource management ([White et al., 2013](#)). However, the completeness and accuracy of the DIM point clouds and LiDAR data were not significantly improved. LiDAR data interpolation aided by images can produce complete and finer point clouds than LiDAR data and does so with the guidance

of image information ([He et al., 2012](#)), but it can also produce unreliable predictions in a large missing area in the point clouds. Dense image matching constrained by LiDAR data is a more reliable method, which uses at least two overlapped images to form a stereo pair and integrates the LiDAR data into an advanced DIM framework ([Huang et al., 2018](#)). The LiDAR data were projected onto the stereo epipolar images through collinearity equations. These projected points are defined as LiDAR projection points, which render sparse laser points with known depths or disparities in an image grid. LiDAR projection points can be used in many aspects of DIM, such as reducing the disparity search range ([Zhou et al., 2018](#)), optimizing the matching cost ([Poggi et al., 2019](#)), and adjusting or adding penalty parameters ([Huber and Kanade, 2011](#)). Applying the aforementioned strategies can improve dense matching results when point clouds are dense. However, when LiDAR point clouds are too sparse, the improvement effect is weak. A reasonable prediction of the disparities of the neighboring pixels can expand the number of LiDAR projection points and improve the dense matching results ([Shivakumar et al., 2019](#)). However, this approach also presents a new challenge in that the dense matching results rely on the accuracy of the predicted disparities.

We propose a novel method of LiDAR-guided stereo matching (LGSM) with a spatial consistency constraint that effectively expands the constraint scopes of sparse LiDAR projection points with the guidance of image information. Our riverbed enhancement function (Subsection 3.3) in our proposed method makes full use of spatial consistency. Its basic assumption is that there are continuous disparity or depth changes in the homogeneous region of an image. The main contributions of this study are as follows:

- (1) We propose a riverbed enhancement function to expand the constraint scopes of sparse LiDAR projection points without predicting the disparities of homogeneous pixels.
- (2) Our proposed method is fully automatic and adaptive to the percentage of LiDAR projection points on an image. Even if the LiDAR projection points are very sparse, the adaptive parameters ensure that the matching accuracy of our method is significantly better than that of the original stereo matching algorithm.
- (3) Our proposed method is suitable for indoor, street, aerial, and satellite image datasets and provides good transferability across semi-global matching (SGM) and AD-Census.

The remainder of this paper is organized as follows: Section 2 overviews related studies. Section 3 describes our LGSM process with a spatial consistency constraint. Section 4 presents the experimental results for the simulated and real datasets. Section 5 concludes this paper by highlighting our contribution to LGSM and its future use.

2. Related Literature

In the last several years, many attempts have been made to fuse LiDAR data and images to produce dense and accurate point clouds. One simple method is the direct integration of LiDAR data and DIM point clouds. Because LiDAR data offer high-precision but sparse features, many scholars have proposed obtaining dense reconstruction by sparse LiDAR data interpolation aided by images. Owing to recent advancements in DIM, LiDAR-constrained dense matching has received substantial attention as well. Therefore, based on the differences in the emphasis of the data sources in the fusion process, the fusion methods of laser range data and images can be classified as follows: 1) point cloud fusion, 2) LiDAR data interpolation aided by images, and 3) DIM constrained by LiDAR data. Figure 1 illustrates the fusion methods of LiDAR data and images, where the continuous lines are key processes, and the dashed lines represent auxiliary processes.

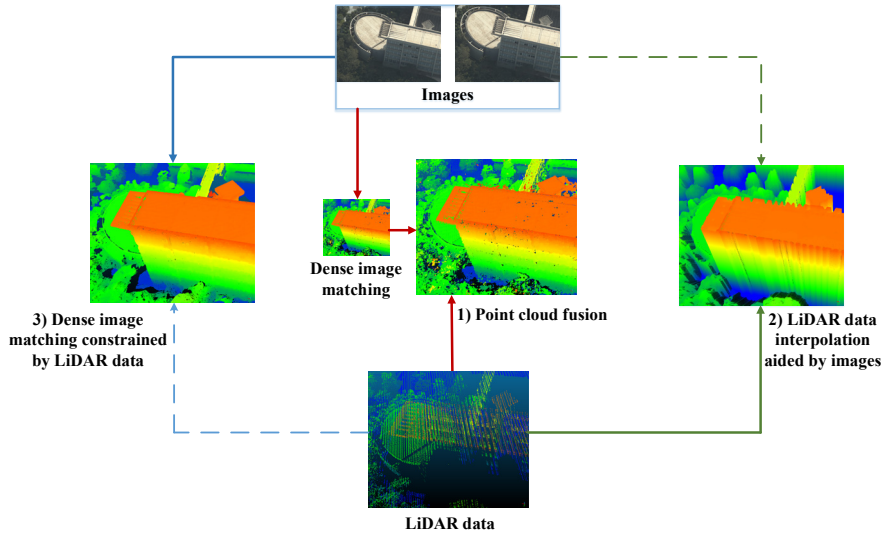


Figure 1. Fusion methods of LiDAR data and images (height of the point cloud from low to high is mapped to the pseudo color from blue to red). Continuous lines are key processes. Dashed lines are auxiliary processes.

2.1 Point cloud fusion

Point cloud fusion directly integrates LiDAR data and DIM point clouds. The synergism of the two data types considerably exceeds the information obtained by individual sensors, which plays an essential role in many geoscience applications. This approach has been used to detect changes and create a series of more robust and complete digital terrain models by combining airborne LiDAR scanning data and aerial imagery ([Schenk and Csathó, 2002](#)). Combining the higher density of the matching point clouds and the higher reliability of LiDAR point clouds can improve the quality of DSM, especially in narrow alleys and courtyards ([Mandlbürger et al., 2017](#)). In forest management, LiDAR data can determine tree height and digital terrain models, and image data that can extract tree species and tree health information are used to create a complete forest resource inventory model ([White et al., 2013](#)). In the field of heritage protection, a combination of LiDAR data and DIM point clouds is used to create a high-resolution 3D model of monuments, statues, or facades ([Schenk and Csathó, 2002](#)). In a large-scale and complicated architectural scene, the images and laser scans are merged with a coarse-to-fine strategy ([Gao et al., 2020](#)) to reconstruct an accurate and complete 3D model (point cloud or surface mesh). Although point cloud fusion is simple and convenient in computation, the completeness and accuracy of DIM point clouds and LiDAR data have not been significantly improved individually, limiting the applications of the type of methods.

2.2 LiDAR data interpolation aided by images

LiDAR data interpolation aided by images combines LiDAR data with a single registered image to estimate the depths of all the points or pixels in the higher-resolution grids after interpolation ([Huang et al., 2018](#)). The image-guided method assumes that most discontinuities in the image of one sensor correspond to discontinuities in the other sensors ([Zomet and Peleg, 2002](#)). The most commonly used image-guided method is the bilateral filter ([Kopf et al., 2007](#)) and its optimization method ([Min et al., 2012](#)). To reduce the computing time of LiDAR data interpolation, a weighted average based on homogeneous pixels is a fast, effective method ([Wang and Ferrie, 2015](#)). Several super-resolution reconstruction methods based on deep learning have outperformed the traditional interpolation method in accuracy and efficiency ([Cui et al., 2021](#); [Eldesokey et al., 2019](#); [Zhang et al., 2019](#)). However, LiDAR data interpolation aided by images is an unreliable predictor in a large missing area in the point clouds.

2.3 DIM constrained by LiDAR data

DIM constrained by LiDAR data first obtains the position of the laser point on the image, which can be regarded as a high-precision control point. Next, the constraints of the LiDAR data were integrated into the dense matching framework. DIM constrained by LiDAR data is advantageous for automated 3D reconstruction because of the complementary characteristics of LiDAR and images ([Nickels et al., 2003](#)). Several studies have used LiDAR data projected on an image as a seed point and then generated a depth or disparity map of the entire image using a region growing algorithm ([Gandhi et al., 2012](#); [Veitch-Michaelis et al., 2015](#)). Other studies have adjusted or added penalty parameters in the cost aggregation process that depend on the distance between the current disparity and the disparity of the LiDAR projection point ([Huang et al., 2018](#); [Huber and Kanade, 2011](#)). This approach performs well in a specific DIM algorithm, but directly applying it to other DIM algorithms is difficult. Reducing the disparity search range for each pixel in an image based on LiDAR data is a general strategy that can improve matching accuracy and efficiency ([Huang et al., 2018](#); [Zhou et al., 2018](#)). The matching accuracy can be further improved by optimizing the cost volume, which stores the matching cost of each pixel in the reference image with the matching image in the disparity range. Directly optimizing the cost volume can be applied to most stereo matching algorithms with a cost volume. The Gaussian enhancement function was used to optimize the cost volume at each LiDAR projection point, which improved the accuracy of dense matching ([Poggi et al., 2019](#)). Furthermore, expanding the LiDAR projection points significantly improved dense matching results by predicting the disparities of the neighboring pixels around the LiDAR projection points ([Shivakumar et al., 2019](#)); however, its matching accuracy relies on the accuracy of the predicted disparities.

To solve the aforementioned limitations, we propose a novel method of LGSM with a spatial consistency constraint that mainly comprises two steps: 1) the spatial neighborhood homogeneous pixels of each LiDAR projection point are detected and 2) the cost volume of these pixels is updated with a specific modulation function. This method can effectively extend LiDAR projection points without predicting the disparities of homogeneous pixels, generating a more robust and accurate disparity map.

3. Methodology

DIM is usually conducted in four steps: cost computation, cost aggregation, disparity computation, and disparity refinement (Scharstein and Szeliski, 2002). After LiDAR outlier removal in Subsection 3.1, the LGSM optimizes the cost volume of LiDAR projection points and homogenous pixels without changing the traditional DIM pipeline. Figure 2 shows the flowchart of LGSM: the black parts are the traditional DIM pipeline, and the red parts are the research focus of this study. First, the homogeneous pixels around the LiDAR projection points are detected from the image based on color or intensity similarity (described in detail in Subsection 3.2). Next, the cost volume is optimized through our novel riverbed enhancement function (defined in detail in Subsection 3.3).

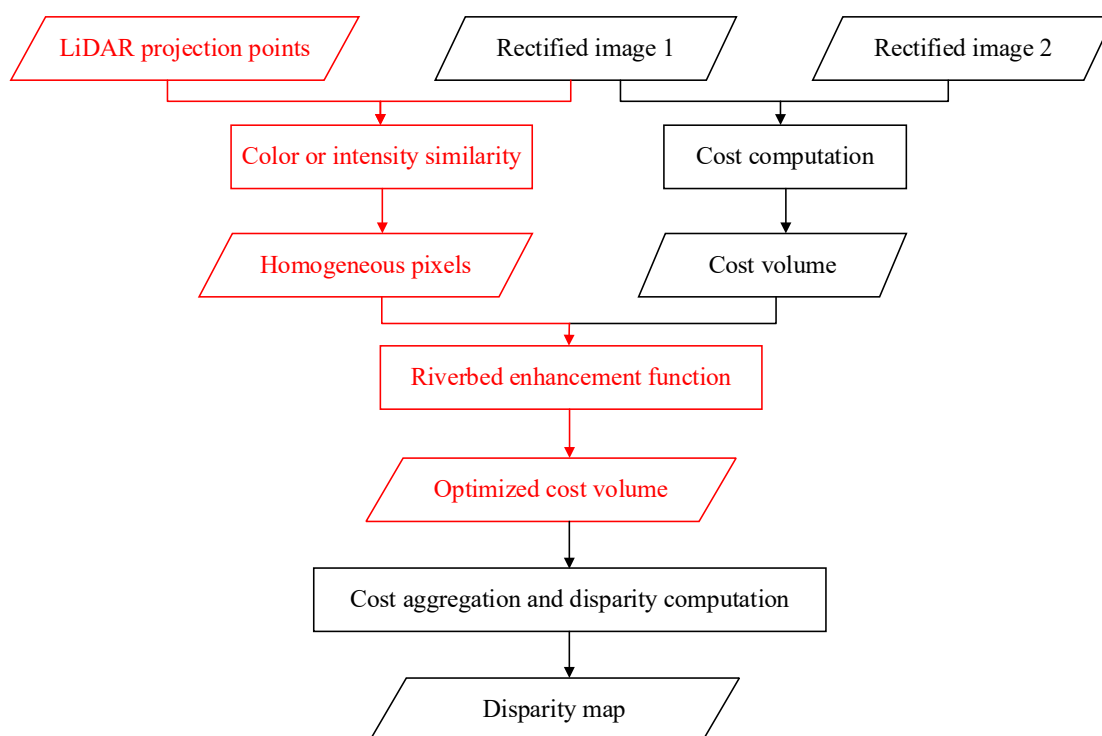


Figure 2. Flowchart of LGSM. The black parts are the traditional DIM pipeline; the red parts are the research focus of this paper.

3.1 LiDAR outlier removal

The positional uncertainty of each LiDAR point is different and is influenced by multiple parameters, such as the sensor-to-object distance, incidence angle, and surface reflectivity. Therefore, selecting suitable points for a dedicated task is an important step (Ozendi et al., 2018).

Various methods have been used to estimate the positional quality of individual LiDAR points ([Chen et al., 2016](#); [Ozendi et al., 2017](#); [Wujanz et al., 2017](#)). Points with large errors are discarded before they can be used in LiDAR data and image fusion.

Additionally, sparse outliers caused by measurement errors and isolated points caused by flying objects or multiple reflections of laser echoes are eliminated using statistical outlier removal (SOR) ([Rusu et al., 2008](#)). This algorithm iterates through the entire input twice: first, a distance threshold is calculated from the average distance between each point and its nearest k neighbors; next, the points are classified as outliers if their average neighbor distance is above this threshold. As shown in Figure 3 (a), there are many LiDAR outliers in the air. Subsequently, as shown in Figure 3 (b), these outliers are filtered out via SOR.

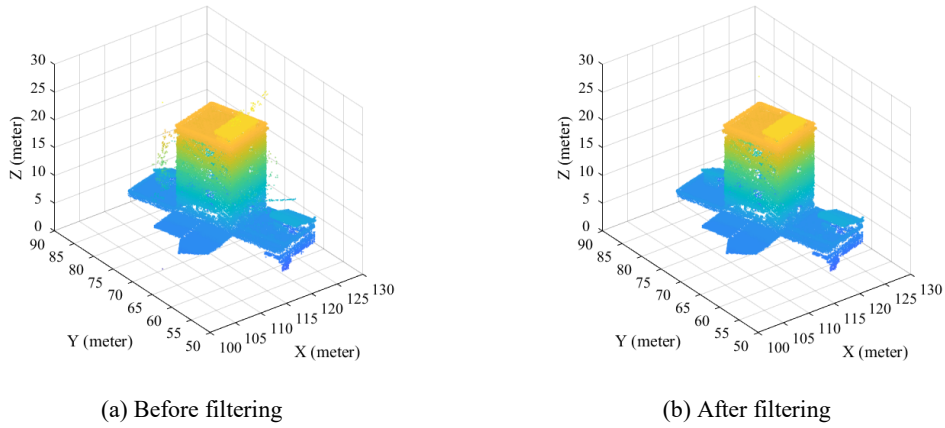


Figure 3. LiDAR outlier removal via SOR. Height of the point cloud from low to high is mapped to the pseudo color from blue to yellow.

3.2 Homogeneous pixels around the LiDAR projection point

Registering the images and LiDAR data is a prerequisite, and generating LiDAR projection points on the image is the initial step of LGSM. In this study, all unregistered data were accurately registered using multi-feature matching ([Wan et al., 2020](#); [Zhang et al., 2015](#)). After accurate registration, LiDAR data are projected onto the left and right rectified images according to the precise orientation parameters of the image. In the process of projection, a simple, fast hidden point removal operator ([Katz et al., 2007](#)) was used to remove occluded point clouds. The operator comprises an inversion and a convex hull construction.

The coordinates of a LiDAR point on the left and right rectified images at this point are (x_L, y_L) and (x_R, y_R) , respectively. Thus the true disparity of (x_L, y_L) is d_m :

$$d_m = x_R - x_L, \quad (1)$$

where (x_L, y_L) is the LiDAR projection point, and d_m is the disparity value corresponding to the LiDAR projection point. The disparity value generated by dense matching should be the same as d_m , which is the basic assumption of LGSM.

Homogeneous pixels are pixels with no significant change in intensity or color values within the spatial neighborhood of the LiDAR projection point. Inspired by the idea of a bilateral filter ([Tomasi et al., 1998](#)), homogeneous pixels are defined as pixels of color or intensity similarity within a certain distance to preserve the shape boundary of the image. We apply this hypothesis by creating a weighted Gaussian distribution based on the spatial and intensity proximities of the centric pixel:

$$W_{(i,j)} = 1 - \exp\left(-\frac{\|(i,j) - (x_L, y_L)\|^2}{2\sigma_{xy}^2} - \frac{(I(i,j) - I(x_L, y_L))^2}{2\sigma_I^2}\right), \quad (2)$$

where (i, j) and (x_L, y_L) are the positions of the current pixel and center pixel; and $I(i, j)$ and $I(x_L, y_L)$ are the intensities of the current and the centric pixel, respectively. The exponent part is always negative, and the value range of $W_{(i,j)}$ is [0-1]. Given the threshold γ , we can obtain similar pixels around the LiDAR projection point:

$$S(x_L, y_L) = \{(i, j) \in Window(x_L, y_L) \mid W_{(i,j)} > \gamma\}, \quad (3)$$

where $S(x_L, y_L)$ stores homogeneous pixels around the LiDAR projection point. $Window(x_L, y_L)$ refers to a square with a center pixel of (x_L, y_L) and a window size of $s \times s$. An illustration of the homogeneous pixels is shown in Figure 4.

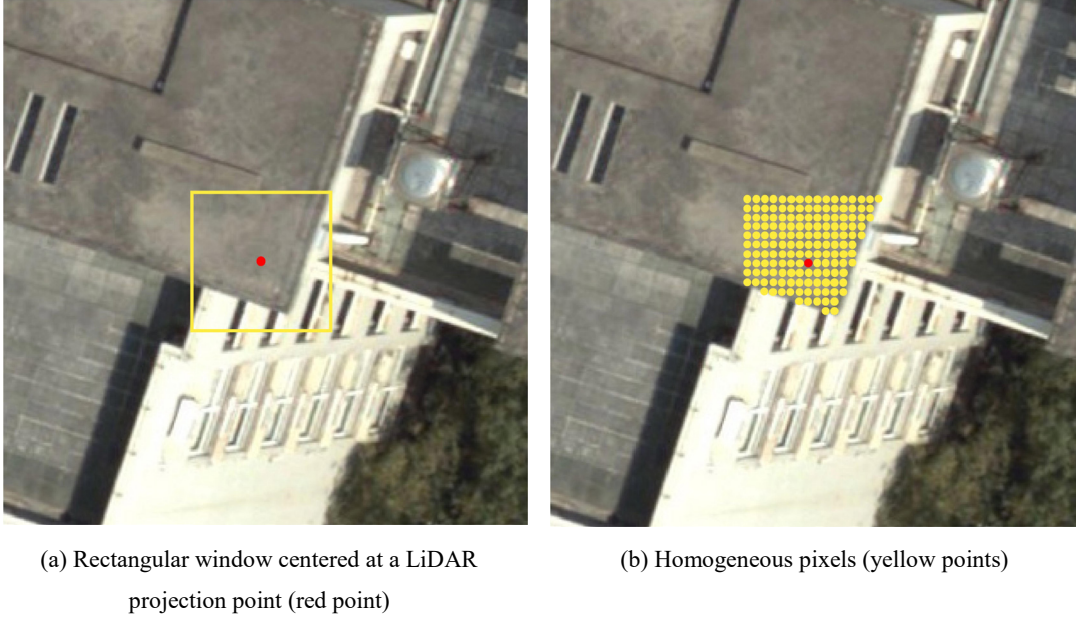


Figure 4. Homogeneous pixels.

Intuitively, the larger the window size, the greater the number of homogeneous pixels near the LiDAR projection point. Reasonable σ_{xy} and γ can ensure that when the pixels are far from the LiDAR projection point, pixels with the same intensity or color will not be judged as homogeneous pixels. Section 4 discusses the recommended values of all parameters, for example, the window size in the formula. When the density of LiDAR points is too high, some pixels in the image may be homogeneous pixels around multiple LiDAR projection points. To ensure that all the pixels in the image are homogenous pixels of at most one LiDAR projection point, we follow three basic rules: 1) $Window(x_L, y_L)$ cannot contain other LiDAR projection points; 2) window size cannot be too large, because the continuous disparity changes of homogeneous pixels are effective in a limited range; and 3) a matrix with the image size is created to ensure that each pixel is at most a homogeneous pixel of one LiDAR projection point.

3.3 LiDAR-constrained cost volume of stereo matching

The first step of the cost computation is to obtain the feature description of each pixel on the left and right images. Next, the matching cost is calculated by measuring the distances of the feature description of the matching point:

$$C((x, y), d) = Dist(I(x, y), J(x + d, y)), \quad (4)$$

where $C((x,y),d)$ represents the matching cost of the current pixel (x,y) with d as the disparity. $I(x,y)$ and $J(x+d,y)$ are the feature descriptions of the matching points of the reference and matching images, respectively. $Dist$ is the similarity measure of the feature descriptions of the matching points, such as the Hamming distance. Cost volume stores the matching cost of each pixel in the reference image with the matching image in the disparity range. It has $H \times W \times D$ dimensions, with $H \times W$ being the resolution of the reference image and D the maximum disparity search range. The cost volume, which runs through cost computation, cost aggregation, and disparity computation, directly influences the results of dense matching. In this paper, the abbreviation for the 3D cost volume of the entire image is F .

Optimizing the cost volume of LiDAR projection points based on the high fidelity of LiDAR data is an effective method to improve the matching accuracy. The Gaussian enhancement function is an excellent method, which fully considers that the closer the LiDAR projection point is to the real disparity, the higher the confidence of the disparity d (Poggi et al., 2019). The Gaussian enhancement function is used to optimize the cost of all disparities within the disparity search range of the LiDAR projection point. When updating the cost volume of the LiDAR point position, the cost corresponding to disparity d_m calculated by the LiDAR data and its neighborhood disparities should be reduced, and the cost of other disparities within the disparity search range should be increased, as shown in Figure 5 (a). The Gaussian enhancement function optimizes the cost volume by selecting a modulation function with a height of k , and the standard error is c , producing an enhanced cost volume G from the initial cost volume F :

$$G = [k * (1 - e^{-\frac{(d-d_m)^2}{2c^2}})] * F. \quad (5)$$

Although the Gaussian enhancement function improves the result of dense matching, the effect of this improvement is limited when the LiDAR points are too sparse. Therefore, simply optimizing the cost volume of LiDAR projection points is insufficient.

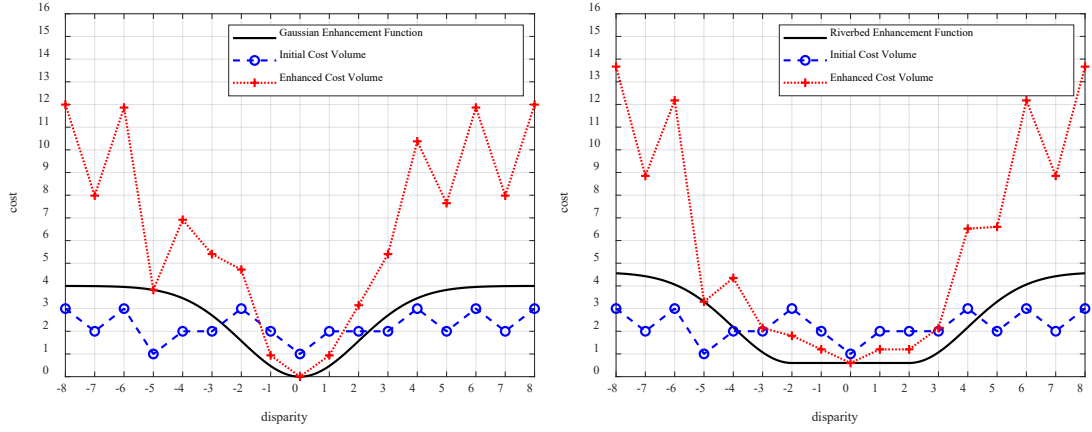
A general hypothesis is that there are continuous disparity or depth changes in the homogeneous region of an image, which has been successfully used by many powerful matching (Hirschmuller, 2005; Huang et al., 2020; Qin, 2019; Yoon and Kweon, 2006) and post-filtering (Huang and Qin, 2020) algorithms. Thus, LiDAR data can be used to constrain the cost volume of not only the

pixel where the LiDAR projection point is located but also the cost volume of the homogeneous neighborhood pixel of the LiDAR projection point. To fully use the LiDAR constraints, the neighborhood information of the LiDAR projection points, and the initial cost volume, in this paper, we introduce a method that is more reliable than that in literature for updating cost volume.

As shown in Figure 5 (b), a function that resembles a riverbed is proposed, called the riverbed enhancement function, and considers the spatial consistency of homogeneous pixels. First, we calculate the similarity $W_{(i,j)}$ between the neighborhood pixel and the LiDAR projection point. Next, we calculate the Euclidean distance w between the neighborhood pixel and the LiDAR projection point. When the disparity of the LiDAR projection point is d_m , the disparity of each homogeneous pixel has a higher confidence between $d_m - w$ and $d_m + w$, and there is lower confidence in other disparities. Thus, the cost volume is uniformly adjusted within the disparity range $(d_m - w, d_m + w)$, and the cost volume is continuously enhanced with a Gaussian model outside the above range.

$$G = \begin{cases} [k * (1 - e^{-\frac{(d-d_m+w)^2}{2c^2}}) + W(i, j)] * F & d \leq d_m - w \\ W(i, j) * F & d_m - w < d < d_m + w \\ [k * (1 - e^{-\frac{(d-d_m-w)^2}{2c^2}}) + W(i, j)] * F & d \geq d_m + w \end{cases} \quad (6)$$

In the aforementioned formula, the similarity of the LiDAR projection points is added to each piecewise function, which effectively guarantees the continuity of the piecewise function. The riverbed enhancement function is equivalent to the Gaussian enhancement function when the pixel is located at the LiDAR projection point (Euclidean distance $w = 0$ and similarity $W_{(i,j)} = 0$). Therefore, the Gaussian enhancement function is a special case of the riverbed enhancement function. The riverbed model is an extension of the Gaussian model and fully uses the continuous disparity or depth changes in the homogeneous region of an image.



(a) Gaussian Enhancement Function

(b) Riverbed Enhancement Function

Figure 5. Modulation function used for cost volume updating: (a) the Gaussian enhancement function is used to enhance the cost volume of LiDAR projection points, and (b) our riverbed enhancement function is used to enhance the cost volume of LiDAR projection points and their homogeneous pixels.

After LiDAR outlier removal and hidden point removal, most outliers and occluded points of the LiDAR data were eliminated. However, inconsistent points between the laser range data and images might remain, for example, blunders and rolling shutter effects. Because LiDAR projection points serve as constraints, inaccurate LiDAR projection points will incorrectly guide DIM. Thus, because these inconsistent points often do not satisfy the photo-consistency constraints in the matching, we use a pyramid matching strategy to detect and remove erroneous LiDAR projection points at the beginning of LGSM.

Pyramid matching for detecting and removing erroneous LiDAR points is effective and sufficient (Huang et al., 2018). If there is no excessive requirement for matching efficiency, the recommended setting is that the size of the pyramid image is half the size of the original image. In the process of downsampling, if several LiDAR projection points correspond to the same image pixel, the point with the maximal disparity is selected because the others are occluded. The disparity d_m must be multiplied by the ratio of the size of the pyramid image to the original image to generate a new disparity d_s . To improve the accuracy of the dense matching of pyramid images, we enhance the matching cost of points, which is far from the disparity of the laser range data:

$$G = [1 + k * (1 - e^{-\frac{(d-d_s)^2}{c^2}})] * F. \quad (7)$$

Equation (5) is similar to Equation (7), but Equation (5) retains the original matching cost for reducing the strong constraints of LiDAR projection points. The optimized matching cost is integrated into global optimization to generate a pyramid image disparity map. The disparity map of the pyramid image was restored to the disparity map corresponding to the original image, and the boundaries were refined through weighted median filtering. We then compared the disparities of LiDAR projection points with the refined disparity map and removed LiDAR projection points with disparity differences of greater than two pixels.

4. Experimental results and discussion

4.1. Experimental settings

The inputs of the LGSM are rectified images and LiDAR data. An overview of the input data is presented in Table 1. Thus, the performance of LGSM is discussed based on various stereo datasets, including indoor, street, satellite, and aerial images. In addition to stereo images, street and aerial stereo image datasets provide LiDAR data, and indoor or satellite stereo image datasets provide reference disparity maps collected by structured lighting scanners or fused DSM. According to the LiDAR data source is LiDAR or the others (e.g. structured lighting scanners, fused DSM), the aforementioned datasets are divided into real and simulated datasets. We simulated the LiDAR projection points on the simulated datasets by randomly sampling the reference disparity map. Different sampling intervals represent different percentages of LiDAR points, which contributes to verifying the degree of influence of LGSM in different LiDAR point percentages. The percentage of LiDAR points refers to the number of pixels of the LiDAR projection points divided by the number of pixels in the image area where the LiDAR projection points are located.

Table 1. Datasets overview.

Dataset	Scene	LiDAR data source	Classification	Percentage of LiDAR points
Middlebury 2014 (Scharstein et al., 2014)	Indoor	Structured lighting scanners	Simulated	0.05%, 0.08%, 0.16%, 0.44%, 1.23%, 11.11%
			Dataset	
SatStereo (Patil et al., 2019)	Satellite	Fused DSM	Simulated	5%
			Dataset	
KITTI 2015 (Menze et al., 2015)	Street	LiDAR	Real Dataset	5%
Guangzhou Stereo	Aerial	LiDAR	Real Dataset	3%

For the experiments, we integrated the LGSM method into SGM ([Hirschmuller, 2008](#)) in Subsections 4.2 and 4.3, considering that SGM offers an excellent trade-off between matching accuracy and computational efficiency. Based on SGM ([Li, 2020](#)), the cost calculation method was census ([Zabih and Woodfill, 1994](#)), and the disparity refinement only used median filtering without left-right consistency check. Integration, in this case, refers to the LGSM being used to optimize the cost volume calculated by the cost calculation. We compared our method with two other state-of-the-art cost volume optimization methods: the Gauss method ([Poggi et al., 2019](#)) and the Diffusion Based method ([Shivakumar et al., 2019](#)). The Gauss method only optimizes the cost volume of the LiDAR projection points, and the Diffusion Based method optimizes the cost volume of the LiDAR projection points and neighboring pixels based on the predicted disparity map. Furthermore, we replaced SGM with AD-Census ([Mei et al., 2011](#)) in Subsection 4.4, to prove the migration performance of LGSM.

All the parameters were fixed in the experimental configuration, except that the window size changed according to the percentage of LiDAR points. Similar to the fast bilateral solver, the default values of σ_{xy} and σ_l in bilateral filtering were 8 ([Barron and Poole, 2016](#)). Corresponding to the aforementioned parameters, the empirical value of the threshold γ was 0.3. A previous study shows that the recommended values of k and c in the modulation function are 10 and 1, respectively ([Poggi et al., 2019](#)).

The accuracy of the dense matching results was calculated according to the remaining LiDAR projection points (the unsampled pixels in the reference disparity map). The average error is the average of the absolute difference between the dense matching disparity d_i and true disparity d_m at the position of the remaining LiDAR projection points. The average error is defined as follows:

$$Avg = \frac{\sum_i^N |d_i - d_m|}{N}. \quad (8)$$

where N

d_i and d_m divided by the number of remaining

LiDAR projection points N .

4.2. Experimental results of simulated datasets

We evaluated the LGSM method first using the Middlebury 2014 dataset ([Scharstein et al., 2014](#)), which provides 23 stereo pairs of indoor scenes and corresponding ground truth data. Five percent of the ground truth data were randomly sampled as the LiDAR constraints, and the remaining 95% of the ground truth data were used to evaluate the matching accuracy. The sampling percentage is consistent with the experiment of the Gauss method, which contributes to the fairness of the comparison. Because the disparity refinement did not use a left-right consistency check, only the LiDAR projection points distributed on the left rectified image were used. The window size was set at 5×5 to optimize the cost volume of pixels as much as possible.

A few example disparity maps are shown in Figure 6: (a) is the left rectified image of stereo matching, (b) is the simulated LiDAR projection points used to constrain stereo matching, (c) is the matching result of the original SGM, (d–f) are the matching results of the SGM with different LiDAR constraints’ strategies, and (g) is the ground truth disparity map. Valid disparities from small to large are mapped to the pseudo color from blue to red, and invalid disparities are mapped to white. All figures are displayed at full resolution, except that Figure (b) is displayed in the form of downsampling for the visual display. The original SGM substantially restored the 3D shape of the object, as shown in Figure 6 (c). However, Figure 6 shows that the original SGM produces the worst object’s boundary among these compared algorithms. With the introduction of LiDAR constraints, the boundary of the disparity map generated by dense matching improved significantly, as shown in Figure 6 (d–f). Objects had finer boundaries when using the LGSM method and the Diffusion Based method than with the other methods because the two methods extend the LiDAR constraints to homogeneous pixels. As shown in the white ellipse area in Figure 6, the disparity map generated by our LGSM method was the most consistent with the ground truth disparity map and produced the least mismatches, reaffirming the observation that the LGSM method effectively improves the matching robustness.

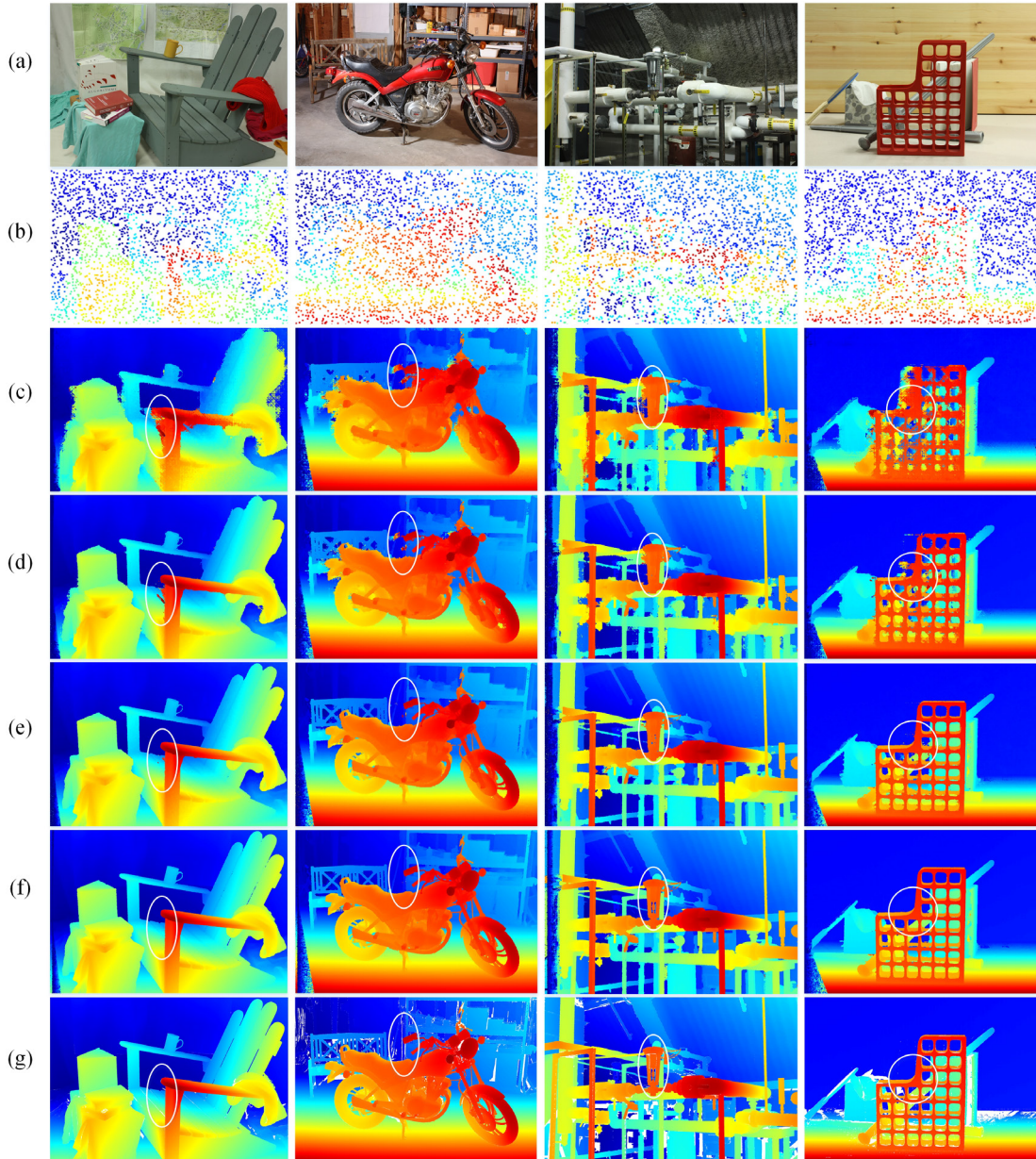


Figure 6. Experimental results for the Middlebury 2014 dataset. (a) Left rectified image; (b) 5% random ground truth disparities; (c) SGM results ([Hirschmuller, 2008](#)); (d) Gauss results ([Poggi et al., 2019](#)); (e) Diffusion Based results ([Shivakumar et al., 2019](#)); (f) LGSM results; (g) Ground truth disparities. Valid disparities from small to large are mapped to the pseudo color from blue to red, and invalid disparities are mapped to white.

We further evaluated the matching accuracy of the Middlebury dataset. As shown in Table 2, the Gauss method, the Diffusion Based method, and the LGSM method were significantly better than the original SGM in all the metrics, and the LGSM method was the best. Numerically, our method was much lower than the original SGM in the number of outliers and the average error: the number

of outliers >2 pixels was reduced from 21.71% to 0.91%, and the average error was reduced from 7.05 to 0.58 pixels.

Table 2. Matching accuracy of original and different LiDAR constraints' SGM for the Middlebury dataset.

Method	$>1\text{px}$	$>2\text{px}$	$>3\text{px}$	Avg/px
SGM	33.07%	21.71%	17.69%	7.05
Gauss	9.35%	3.88%	2.93%	1.56
Diffusion Based	11.81%	2.07%	1.15%	0.98
LGSM	1.93%	0.91%	0.71%	0.58

In Subsection 4.1, window size is the only parameter specified in the LGSM. Window size is the edge length of a square centered on each LiDAR projection point, which limits the initial range of the homogeneous pixels. The window length and width are usually odd numbers, such as 3×3 , 5×5 , 7×7 , 9×9 , 11×11 , 13×13 , 15×15 , 17×17 , and 19×19 . For taking full advantage of the constraints of LiDAR data, the optimal solution is to optimize the cost volume of each pixel. To achieve this goal, the window size multiplied by the percentage of LiDAR points should be greater than or equal to 1 as much as possible. Therefore, we randomly sampled $1:3 \times 3$, $1:9 \times 9$, $1:15 \times 15$, $1:25 \times 25$, $1:35 \times 35$, $1:45 \times 45$, and $1:\infty \times \infty$ of the ground truth data as the LiDAR constraints. Among them, $1:3 \times 3$ indicated that the percentage of LiDAR points was 11.11%, and $1:\infty \times \infty$ indicated that there was no LiDAR point.

Figure 7 shows the relationship between the window size and average error for different percentages of LiDAR points. As shown by the lowest line where the percentage of LiDAR points was $1:3 \times 3$ (11.11%; Figure 7), we marked the average error corresponding to different window sizes. The average error was the smallest when the window size was 5×5 . As the window size increased, the average error gradually increased and tended to be stable. When the percentage of LiDAR points was 0.16%, the matching accuracy of our method achieved a subpixel level, and the original SGM was 3.4 pixels. Although the percentage of LiDAR points was $1:45 \times 45$ (0.05%), the average error of LGSM was more than 50% lower than that of the original SGM. The lowest average error of all the percentages of LiDAR points lead us to two conclusions: 1) the accuracy of the dense matching results increased with the increase in the percentage of LiDAR points, and 2) when the

window size was slightly larger than the ratio of the image to the LiDAR resolution, the average error tended to be stable and remained at a low level. Theoretically, the window size multiplied by the percentage of LiDAR points is approximately equal to one to realize an optimized volume of each pixel in the image. As shown in Figure 7, the window size multiplied by the percentage of LiDAR points must be slightly greater than 1, which considers the uneven distribution of the LiDAR points and homogeneous pixels. Thus, the aforementioned approach ensures that the cost volume of each pixel is optimized as much as possible, and the LiDAR projection point only optimizes the cost volume of its homogeneous pixels.

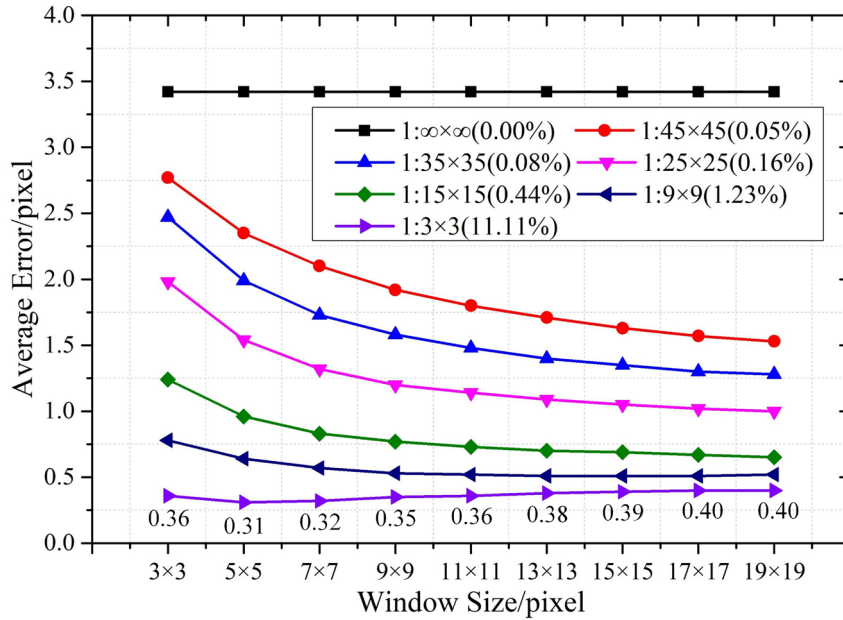


Figure 7. Relationship between window size and average error for different percentages of LiDAR points.

We used the satellite stereo pair dataset provided by Purdue University to verify the effectiveness of LGSM on satellite stereo pairs (Patil et al., 2019). This dataset consists of stereo rectified image pairs collected by WorldView-2 and WorldView-3 and the ground truth disparities for each pixel in a reference image. The disparities are ground truth by first constructing a fused DSM from the stereo pairs and then aligning the LiDAR with the fused DSM. However, the ground truth disparity map retains a small number of outliers, which are commonly observed at the boundaries of buildings.

We randomly sampled 5% of the ground truth disparities as LiDAR constraints. The matching accuracy was evaluated using the remaining 95% of the ground truth data (Table 3). A few example

disparity maps are shown in Figure 8. In the disparity map of the original SGM, there was no obvious disparity change at the boundaries of the buildings. There were slightly improved building boundaries in the Gauss results, but the results for our LGSM method and the Diffusion Based method were closer to the ground truth. In Table 3, the LiDAR-constrained cost volume was significantly better than that of the original SGM in all metrics on the WorldView-2 and WorldView-3 datasets, and the LGSM method produced the best results. Our method reduced the number of outliers 50% more than the original SGM and reduced the average error by 67%.

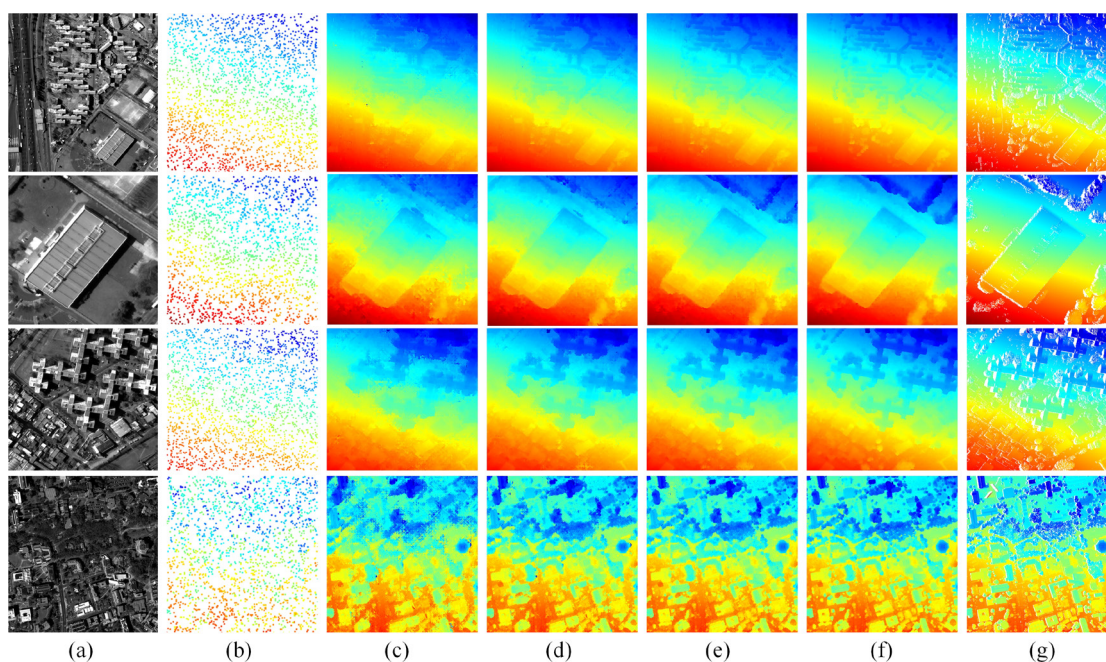


Figure 8. Experimental results for the optical stereo satellite dataset. (a) Left rectified image; (b) 5% random ground truth disparities; (c) SGM results; (d) Gauss results; (e) Diffusion Based results; (f) LGSM results; (g) Ground truth disparities. Valid disparities from small to large are mapped to the pseudo color from blue to red, and invalid disparities are mapped to white.

Table 3. Matching accuracy of original and different LiDAR constraints’ SGM on WorldView-2 and WorldView-3 datasets.

Method	WorldView-2				WorldView-3			
	>1px	>2px	>3px	Avg/px	>1px	>2px	>3px	Avg/px
SGM	70.41%	40.40%	29.02%	3.01	55.80%	36.45%	28.39%	4.47
Gauss	46.70%	21.37%	13.67%	1.74	38.05%	21.33%	15.86%	2.66
Diffusion Based	53.22%	17.40%	8.35%	1.46	41.90%	17.65%	10.85%	2.27
LGSM	31.60%	8.76%	3.91%	0.98	26.17%	10.25%	5.88%	1.52

4.3. Experimental results of real datasets

We also evaluated the performance of LGSM by using the KITTI 2015 dataset ([Menze et al., 2015](#); [Menze et al., 2018](#)), which comprises 200 stereo pairs of street scenes and the corresponding ground truth data. The ground truth data are not pixel-wise in the grayscale image but an accumulation of LiDAR points over a range of frames before and after the reference image. Our experiment used a subset of the ground truth data as sparse depth input along with the stereo pair, and the evaluation was conducted outside the sample set.

We randomly sampled 5% of the ground truth data as LiDAR constraints, and the remaining 95% was used to evaluate the matching accuracy. The window size was set at 5×5 , according to the principle of parameter adaptation in Subsection 4.2. A few example disparity maps are shown in Figure 9, in which our LGSM method outperformed the other two methods. In particular, the disparity map generated by our LGSM method was smoother with fewer false matching points and had more accurate boundaries of objects, such as cars and tree trunks. Notably, the disparity map generated by the LGSM method was similar to that generated by the Diffusion Based method. The disparity maps were similar because both methods expand the constraint scopes of the LiDAR projection points, but their results differed because they used different constraint strategies. Under low light conditions (column 1, Figure 9), the results for the original SGM algorithm were almost completely incorrect. However, all the LiDAR-constrained cost volume methods generated more realistic disparity maps in the LiDAR area, and the results of LGSM were the closest to the ground truth.

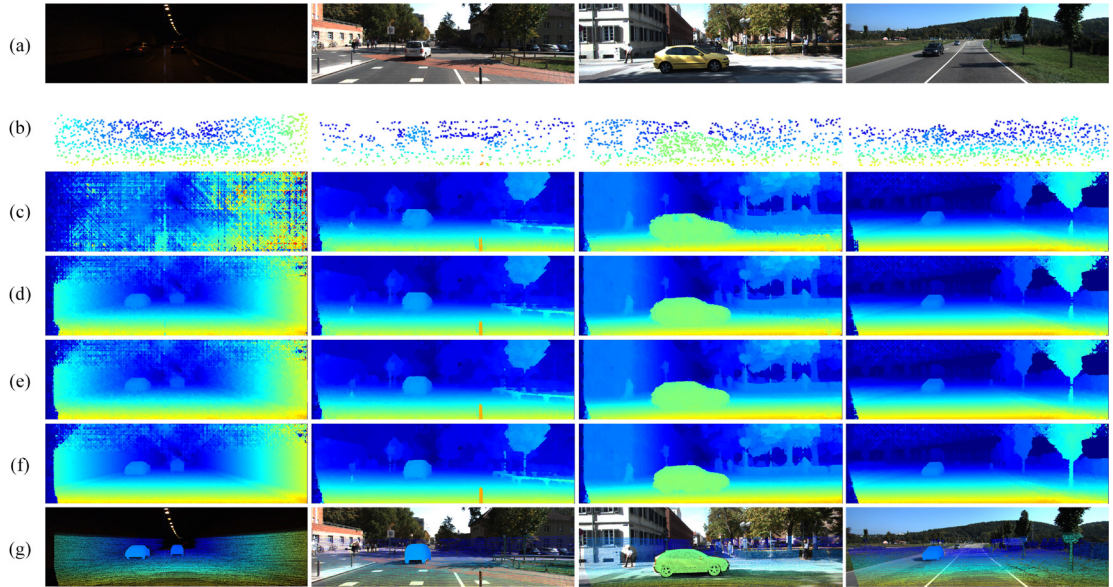


Figure 9. Experimental results for the KITTI 2015 dataset. (a) Left rectified image; (b) 5% random ground truth disparities; (c) SGM results; (d) Gauss results; (e) Diffusion Based results; (f) LGSM results; (g) Ground truth disparities. Valid disparities from small to large are mapped to the pseudo color from blue to red, and invalid disparities are mapped to white.

Table 4 presents the quantitative evaluation results for the KITTI datasets. We confirmed that the Gauss method, the Diffusion Based method, and the LGSM method were significantly better than the original SGM in all the metrics, and the LGSM method produced the best results. For the KITTI 2015 dataset, our LGSM method dramatically improved performances in the number of outliers and average error: the LGSM method reduced the number of outliers >1 , >2 , and >3 pixels by more than 80% than the original SGM; and it reduced the outliers by more than 50% than the Gauss method and the Diffusion Based.

Table 4. Matching accuracy of original and different LiDAR constraints' SGM on the KITTI dataset.

Method	$>1\text{px}$	$>2\text{px}$	$>3\text{px}$	Avg/px
SGM	16.41%	9.69%	6.66%	1.34
Gauss	7.72%	3.76%	2.51%	0.78
Diffusion Based	8.24%	2.74%	1.53%	0.74
LGSM	2.60%	1.06%	0.73%	0.45

We used aerial imagery and LiDAR data for Guangzhou, China, to verify the effectiveness of LGSM on aerial stereo pairs. The ground resolution of the aerial images was approximately 3.2cm, and the LiDAR point density was approximately 30 points/m². According to the selection principle of the window size shown in Subsection 4.1, because the percentage of LiDAR points is close to 3%, we set the window size to 5×5.

Figure 10 shows a few example depth maps obtained using the SGM and different cost volume optimization methods. The upper and lower depth maps correspond to the flat land and urban area, respectively. The disparity map generated by SGM was generally accurate, except for some outliers in difficult matching areas, such as shadows, trees, and buildings. In Figure 10, the outliers of the depth map gradually decreased from left to right, and our LGSM method produced the best results.

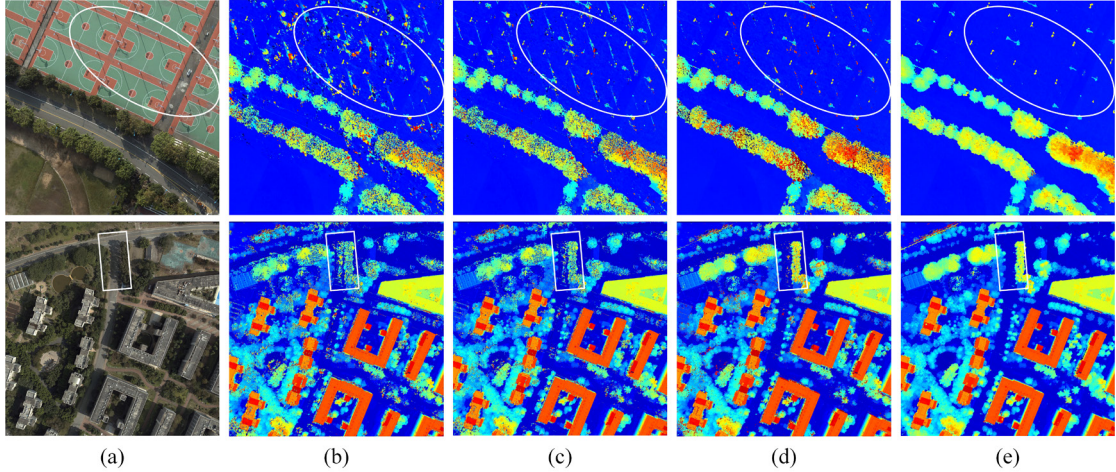


Figure 10. Experimental results for the Guangzhou Stereo Dataset. (a) Left rectified image; (b) SGM results; (c) Gauss results; (d) Diffusion Based results; (e) LGSM results. Depths from low to high are mapped to the pseudo color from blue to red.

Mismatches in difficult matching areas are an urgent problem that must be solved in stereo matching. As illumination changes, the lamppost's shadow is different in the stereo image acquired on different flight belts. This phenomenon could have easily caused pixels on the shadow to be regarded as matching points in the dense matching process and further led to the appearance of striped elevation lines on the flat basketball court, as shown in Figure 10 (b), (c), and (d). The surface shadows of trees on the road also caused the shadow areas to fail to match. However, the introduction

of LiDAR constraints effectively reduced the false interference of shadows on dense matching, as shown in the results of the LGSM in Figure 10 (e). The aforementioned analysis confirms the excellent performance of the LGSM for restoring the height of flat shadows. However, when shadows cannot be distinguished by homogeneous pixels and height changes significantly, our method can only restore the height of LiDAR projection points. This result is equivalent to keeping the LiDAR points in the shaded area without considering the results of dense matching.

In addition to shadow areas, low-texture and repeated texture areas, such as trees, grass, and building areas, caused mismatches as shown in Figure 10 (b), (c), and (d); however, our LGSM method produced more accurate matches, as shown in Figure 10 (e). In summary, the LGSM method improved the matching results in shadows, low texture, and repeated texture regions, which is an important limitation of current stereo matching algorithms.

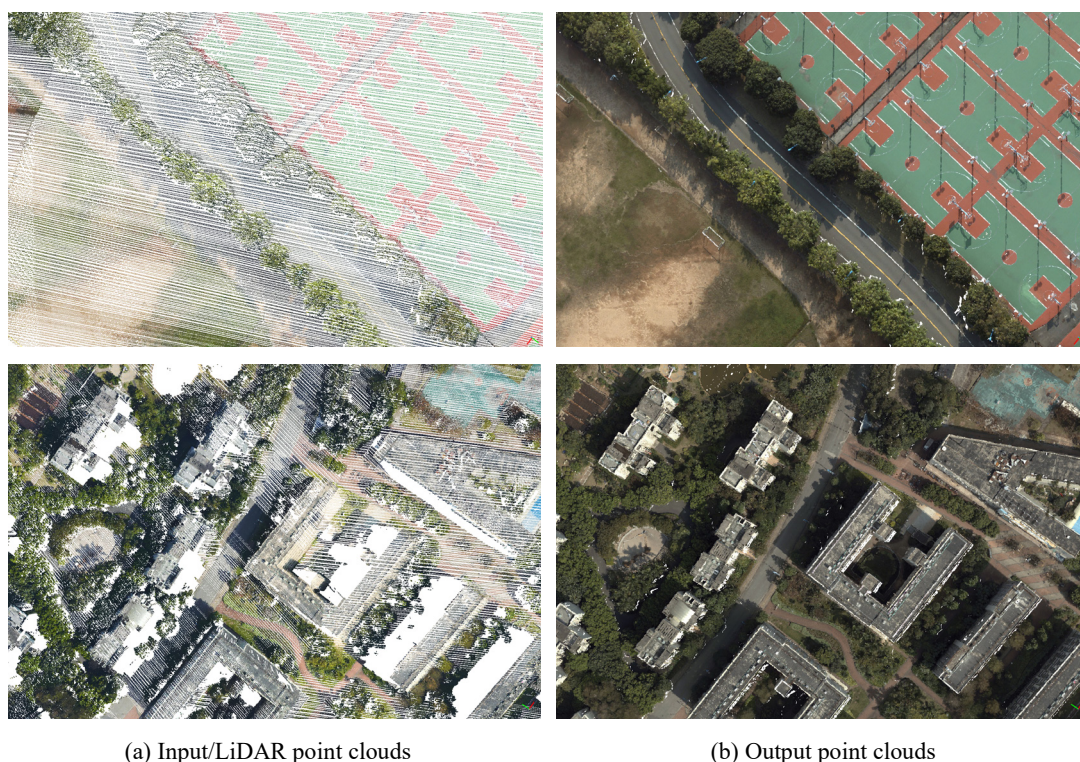


Figure 11. Input and output point clouds of LGSM (background color is white).

The input and output point clouds of LGSM in Figure 11 are at the same viewing angle, which is approximately vertical to the ground. Figure 11 (a) shows that the input/LiDAR point clouds are sparse and unevenly distributed. Figure 11 (b) shows that the output point clouds of the LGSM were

dense and accurate, such as streetlights, basketball hoops, and building boundaries. More notably, the input/LiDAR point clouds were missing in local areas, whereas the output point clouds of the LGSM recovered most of the missing point clouds. Therefore, as shown in Figures 10 and 11, the complementary fusion of LiDAR data and stereo images can produce high-precision and high-density point clouds via our LGSM method.

4.4. Migration analysis

To prove that our LGSM method can produce good results even with different stereo matching algorithms, we evaluated it using the AD-Census algorithm instead of the SGM algorithm. The AD-Census comprises four steps: 1) AD-Census cost initialization, 2) cross-based cost aggregation, 3) scanline optimization, and 4) multi-step disparity refinement. AD-Census is integrated into the real-time stereo matching of Intel RealSense D400 because of its extremely high matching efficiency ([Keselman et al., 2017](#)). Based on AD-Census ([Li, 2021](#)), we applied the LiDAR-constrained cost volume before the scanline optimization. We did not adjust any parameters, which was consistent with the optimization strategy of the SGM algorithm.

As for any prior experiments, we randomly sampled the sparse inputs described in Subsections 4.2 and 4.3 and obtained an average percentage of LiDAR points below 5%. Table 5 compares AD-Census and its cost volume optimization using sparse input cues on Middlebury 2014 (left) and KITTI 2015 (right). Middlebury 2014 (left) and KITTI 2015 represent the simulated and real datasets, respectively. For both datasets, the Gauss method, the Diffusion Based method, and the LGSM method were significantly better than the original AD-Census in all metrics, and our LGSM method produced the best result. For Middlebury 2014 dataset, the LGSM method produced a few tenths of the number of outliers and the average error of that of the original AD-Census: we reduced the number of outliers by >3 pixels from 25.77% to 2.00%, and the average error was reduced from 15.36 to 0.98. For KITTI 2015 dataset, the LGSM method also dramatically improved the number of outliers and the average error. Specifically, our LGSM method reduced the number of outliers by >1 , >2 , and >3 pixels by more than 90% than the original AD-Census, and our LGSM method reduced the number of outliers by more than 50% than the two other methods. More importantly, among all the methods, only our LGSM method reduced the average error to a subpixel level.

Evaluations with AD-Census and the aforementioned SGM confirm that the LGSM method can

be regarded as a general-purpose LiDAR-guided stereo matching solution capable of significant improvements using different stereo matching algorithms.

Table 5. Matching accuracy of original and different LiDAR constraints’ AD-Census on the Middlebury and KITTI datasets.

Method	Middlebury 2014				KITTI 2015			
	>1px	>2px	>3px	Avg/px	>1px	>2px	>3px	Avg/px
AD-Census	40.75%	29.86%	25.77%	15.36	29.32%	21.06%	15.64%	3.34
Gauss	8.57%	6.38%	5.68%	3.98	6.85%	4.35%	3.63%	1.24
Diffusion Based	8.73%	4.99%	4.32%	3.19	7.05%	3.56%	2.89%	1.18
LGSM	4.07%	2.54%	2.00%	0.98	2.88%	1.03%	0.75%	0.53

4.5. Discussion

In this subsection, we discuss how to manage LiDAR point clouds with outliers and inaccurate registration between the images and LiDAR point clouds. If the calibration accuracy of the laser scanner is known and the error ellipse of each LiDAR point is calculated, LiDAR points with larger errors are removed. In this study, LiDAR points with large errors were filtered out by the LiDAR data provider. Additionally, sparse outliers caused by measurement errors and isolated points caused by flying objects or multiple reflections of laser echoes are eliminated through the SOR.

In the Guangzhou dataset, LiDAR point clouds are the result of multi-station data combinations. Therefore, when point clouds are projected onto an image, occlusion is a common phenomenon. On the roof of the building, the disparities of the LiDAR projection points slowly change. However, as shown in the top image of Figure 12 (a), the occlusion caused many inaccurate LiDAR projection points. In the process of projection, occluded point clouds were removed via the hidden point removal operator, shown in the top image of Figure 12 (b). Finally, only the cleaned LiDAR projection points remained on the image, shown in the top image of Figure 12 (c).

The aforementioned LiDAR outlier removal and occlusion detection methods removed most of the noise from LiDAR projection points. In addition, our LGSM method can tolerate the presence of noise, because the method has a process for detecting and eliminating inaccurate LiDAR projection points (described in Subsection 3.3). In the middle and bottom images of Figure 12 (a), there were inaccurate LiDAR projection points in the white ellipse, mainly caused by the

measurement errors of the laser scanner and rolling shutter effects. Inaccurate LiDAR projection points were removed via pyramid matching, and only the cleaned LiDAR projection points remained on the image, shown in the middle and bottom images of Figure 12 (c).

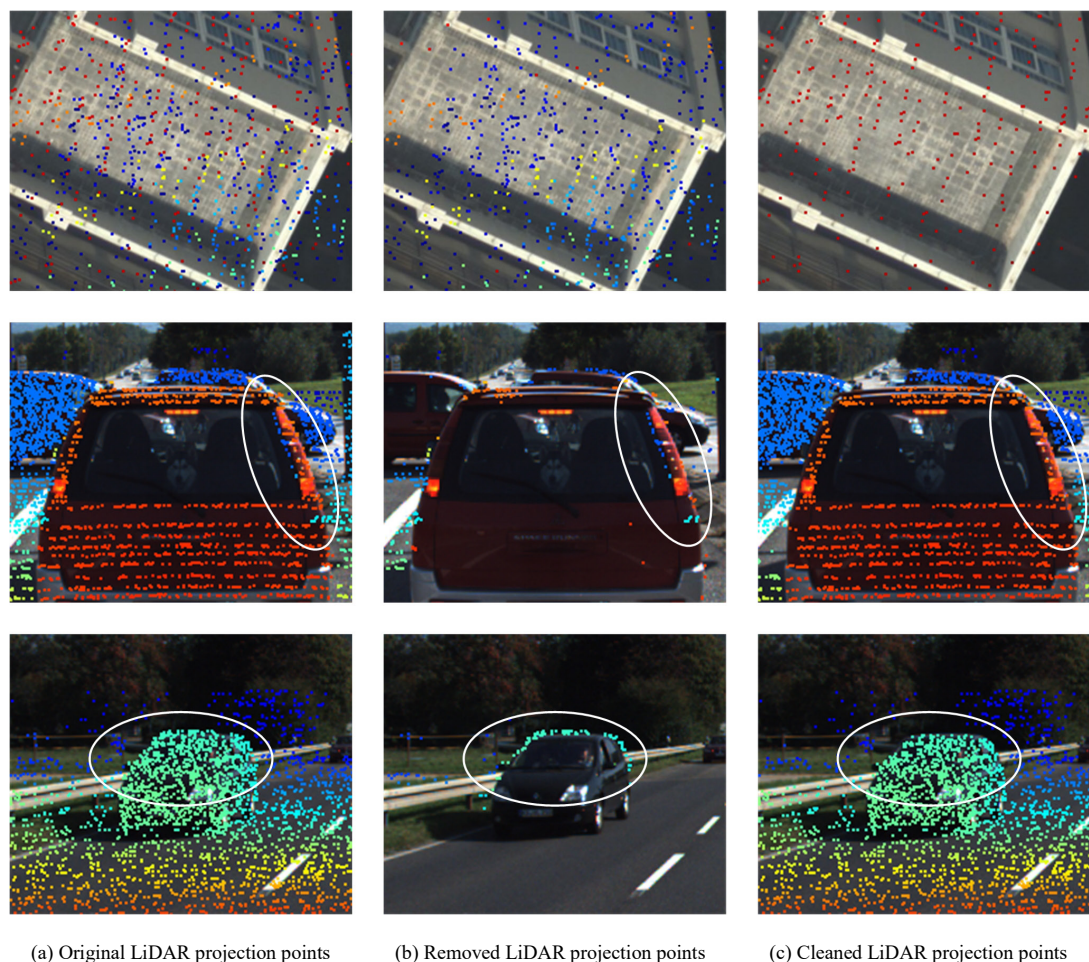


Figure 12. Outlier elimination of LiDAR projection points. Valid disparities from small to large are mapped to the pseudo color from blue to red and are superimposed onto the RGB image.

When the images and LiDAR point clouds are only coarsely registered, the DIM point clouds and LiDAR point clouds also have a significant offset. Coarse registration leads to a significant decrease in the matching accuracy of most DIMs constrained by LiDAR data. Accurate registration is a prerequisite for most LiDAR and image fusion methods, including the LGSM method. We have achieved highly accurate registration of the images and LiDAR point clouds from our prior research ([Wan et al., 2020](#); [Zhang et al., 2015](#)). The registration accuracy in both the horizontal and vertical directions was very close to the ranging accuracy of the LiDAR sensor and the ground sampling

distance of the image.

5. Conclusions

In this paper, we propose a novel LGSM method that considers continuous disparity or depth changes in the homogeneous region of an image to generate high-precision and high-density point clouds. The experimental results verify that the LGSM method is suitable for various stereo datasets, such as indoor, street, aerial, and satellite images. Furthermore, qualitative and quantitative evaluations confirm that our LGSM method is superior to two state-of-the-art methods, especially in reducing mismatches in difficult matching areas and refining the boundaries of objects.

Window size selection is a fully automatic process in our proposed LGSM method and is adaptive to the percentage of LiDAR projection points on the image. When the percentage of LiDAR points was 0.16%, the matching accuracy of LGSM achieved a subpixel level, and the original stereo matching algorithm was 3.4 pixels. To verify the adaptability of the LGSM, we applied the AD-Census algorithm instead of the original SGM algorithm. The LGSM method also achieved significant improvement, which further enhanced its application value and potential utilization. For example, under low light conditions, our LGSM method produced better results than the original stereo matching strategy, which would facilitate improvement in the 3D perception ability of autonomous vehicles.

This study confirms that the proposed LGSM method is suitable for the fusion of stereo images and LiDAR data. We plan to extend our method in further research to multi-view images or sparse signals from sources not used in this paper, for example, radar, feature matching, and time-of-flight range cameras.

Acknowledgments

We would like to thank the editors and the anonymous reviewers for their comments and contributions, Dr. Yingsong Li for providing the source code of SGM and AD-Census, and Guangzhou Jiantong Surveying and Mapping Geoinformation Technology Co., Ltd for providing the Guangzhou Stereo Dataset. This work was supported in part by the Basic Research Strengthening Program of China (173 Program) with project number 2020-JCJQ-ZD-015-00-04,

and the National Natural Science Foundation of China with project number 41871368.

References

- Arnold, E., Al-Jarrah, O.Y., Dianati, M., Fallah, S., Oxtoby, D., Mouzakitis, A., 2019. A Survey on 3D Object Detection Methods for Autonomous Driving Applications. *IEEE Transactions on Intelligent Transportation Systems* 20, 3782-3795.
- Barron, J.T., Poole, B., 2016. The fast bilateral solver, *European Conference on Computer Vision*. Springer, pp. 617-632.
- Chen, X.J., Zhang, G., Hua, X.H., Xuan, W., 2016. An Average Error-Ellipsoid Model for Evaluating TLS Point-Cloud Accuracy. *The Photogrammetric Record* 31, 71-87.
- Cui, Y., Chen, R., Chu, W., Chen, L., Tian, D., Li, Y., Cao, D., 2021. Deep learning for image and point cloud fusion in autonomous driving: A review. *IEEE Transactions on Intelligent Transportation Systems*, 1-18.
- Eldesokey, A., Felsberg, M., Khan, F.S., 2019. Confidence propagation through cnns for guided sparse depth regression. *IEEE transactions on pattern analysis and machine intelligence* 42, 2423-2436.
- Gandhi, V., Cech, J., Horaud, R., Ieee, 2012. High-Resolution Depth Maps Based on TOF-Stereo Fusion, 2012 IEEE International Conference on Robotics and Automation, pp. 4742-4749.
- Gao, X., Shen, S., Zhu, L., Shi, T., Wang, Z., Hu, Z., 2020. Complete Scene Reconstruction by Merging Images and Laser Scans. *IEEE Transactions on Circuits and Systems for Video Technology* 30, 3688-3701.
- He, K., Sun, J., Tang, X., 2012. Guided image filtering. *IEEE transactions on pattern analysis and machine intelligence* 35, 1397-1409.
- Hirschmuller, H., 2005. Accurate and efficient stereo processing by semi-global matching and mutual information, 2005 IEEE Computer Society Conference on Computer Vision and Pattern Recognition (CVPR'05). IEEE, pp. 807-814.
- Hirschmuller, H., 2008. Stereo processing by semiglobal matching and mutual information. *IEEE transactions on pattern analysis and machine intelligence* 30, 328-341.
- Hu, Z., Hou, Y., Tao, P., Shan, J., 2021. IMGTR: Image-triangle based multi-view 3D reconstruction for urban scenes. *ISPRS Journal of Photogrammetry and Remote Sensing* 181, 191-204.
- Huang, X., Qin, R., 2020. Post-filtering with surface orientation constraints for stereo dense image matching. *The Photogrammetric Record* 35, 375-401.
- Huang, X., Qin, R., Xiao, C., Lu, X., 2018. Super resolution of laser range data based on image-guided fusion and dense matching. *ISPRS Journal of Photogrammetry and Remote Sensing* 144, 105-118.
- Huang, X., Wan, X., Peng, D., 2020. Robust Feature Matching with Spatial Smoothness Constraints. *Remote Sensing* 12, 3158.
- Huber, D., Kanade, T., 2011. Integrating lidar into stereo for fast and improved disparity computation, 2011 International Conference on 3D Imaging, Modeling, Processing, Visualization and Transmission. IEEE, pp. 405-412.
- Katz, S., Tal, A., Basri, R., 2007. Direct visibility of point sets. *ACM Transactions on Graphics* 26.
- Keselman, L., Woodfill, J.I., Grunnet-Jepsen, A., Bhowmik, A., Ieee, 2017. Intel (R) RealSense (TM) Stereoscopic Depth Cameras, 2017 IEEE Conference on Computer Vision and Pattern Recognition Workshops, pp. 1267-1276.
- Kopf, J., Cohen, M.F., Lischinski, D., Uyttendaele, M., 2007. Joint bilateral upsampling. *ACM*

- Transactions on Graphics 26, 96–es.
- Landeschi, G., 2018. Rethinking GIS, three-dimensionality and space perception in archaeology. *World Archaeology* 51, 17-32.
- Li, Y., 2020. SemiGlobalMatching, <https://github.com/ethan-li-coding/SemiGlobalMatching>.
- Li, Y., 2021. AD-Census, <https://github.com/ethan-li-coding/AD-Census>.
- Liu, K., Ma, H., Ma, H., Cai, Z., Zhang, L., 2020. Building Extraction from Airborne LiDAR Data Based on Min-Cut and Improved Post-Processing. *Remote Sensing* 12, 2849.
- Maltezos, E., Kyrkou, A., Ioannidis, C., 2016. LIDAR vs dense image matching point clouds in complex urban scenes, Fourth International Conference on Remote Sensing and Geoinformation of the Environment (RSCy2016). International Society for Optics and Photonics, p. 96881P.
- Mandlburger, G., Wenzel, K., Spitzer, A., Haala, N., Glira, P., Pfeifer, N., 2017. IMPROVED TOPOGRAPHIC MODELS VIA CONCURRENT AIRBORNE LIDAR AND DENSE IMAGE MATCHING, *ISPRS Annals of Photogrammetry, Remote Sensing & Spatial Information Sciences*, pp. 259-266.
- Mei, X., Sun, X., Zhou, M., Jiao, S., Wang, H., Zhang, X., 2011. On Building an Accurate Stereo Matching System on Graphics Hardware, 2011 IEEE International Conference on Computer Vision Workshops. IEEE, pp. 467-474.
- Menze, M., Geiger, A., Ieee, 2015. Object Scene Flow for Autonomous Vehicles, 2015 IEEE Conference on Computer Vision and Pattern Recognition, pp. 3061-3070.
- Menze, M., Heipke, C., Geiger, A., 2018. Object Scene Flow. *ISPRS Journal of Photogrammetry and Remote Sensing* 140, 60-76.
- Min, D., Lu, J., Do, M.N., 2012. Depth video enhancement based on weighted mode filtering. *IEEE Transactions on Image Processing* 21, 1176-1190.
- Moisan, E., Heinkele, C., Foucher, P., Charbonnier, P., Grussenmeyer, P., Guillemin, S., Koehl, M., 2021. Combining Photogrammetric and Bathymetric Data to Build a 3D Model of a Canal Tunnel. *The Photogrammetric Record* 36, 202-223.
- Nefti-Meziani, S., Manzoor, U., Davis, S., Pupala, S.K., 2015. 3D perception from binocular vision for a low cost humanoid robot NAO. *Robotics and Autonomous Systems* 68, 129-139.
- Nickels, K.M., Castano, A., Cianci, C., 2003. Fusion of lidar and stereo range for mobile robots, *Proceedings of the 11th International Conference on Advanced Robotics*. Univ Coimbra, Fac Ciencias & Technol, Coimbra, pp. 65-70.
- Ozendi, M., Akca, D., Topan, H., 2017. A Generic Point Error Model for TLS Derived Point Clouds, *Conference on Videometrics, Range Imaging, and Applications XIV*. Spie-Int Soc Optical Engineering, Munich, GERMANY.
- Ozendi, M., Akca, D., Topan, H., 2018. STOCHASTIC SURFACE MESH RECONSTRUCTION. *International Archives of Photogrammetry Remote Sensing and Spatial Information Sciences XLII-2*, 805-812.
- Paris, C., Bruzzone, L., 2014. A three-dimensional model-based approach to the estimation of the tree top height by fusing low-density LiDAR data and very high resolution optical images. *IEEE Transactions on Geoscience and Remote Sensing* 53, 467-480.
- Patil, S., Comandur, B., Prakash, T., Kak, A.C., 2019. A new stereo benchmarking dataset for satellite images. *arXiv:1907.04404*.
- Poggi, M., Pallotti, D., Tosi, F., Mattoccia, S., 2019. Guided stereo matching, *Proceedings of the IEEE/CVF Conference on Computer Vision and Pattern Recognition*, pp. 979-988.

- Qin, R., 2019. A critical analysis of satellite stereo pairs for digital surface model generation and a matching quality prediction model. *ISPRS Journal of Photogrammetry and Remote Sensing* 154, 139-150.
- Remondino, F., Spera, M.G., Nocerino, E., Menna, F., Nex, F., 2014. State of the art in high density image matching. *The Photogrammetric Record* 29, 144-166.
- Rusu, R.B., Marton, Z.C., Blodow, N., Dolha, M., Beetz, M., 2008. Towards 3D Point cloud based object maps for household environments. *Robotics and Autonomous Systems* 56, 927-941.
- Salvi, J., Pagès, J., Batlle, J., 2004. Pattern codification strategies in structured light systems. *Pattern Recognition* 37, 827-849.
- Scharstein, D., Hirschmüller, H., Kitajima, Y., Krathwohl, G., Nešić, N., Wang, X., Westling, P., 2014. High-Resolution Stereo Datasets with Subpixel-Accurate Ground Truth, in: Jiang, X., Hornegger, J., Koch, R. (Eds.), *Pattern Recognition*, pp. 31-42.
- Scharstein, D., Szeliski, R., 2002. A taxonomy and evaluation of dense two-frame stereo correspondence algorithms. *International Journal of Computer Vision* 47, 7-42.
- Schenk, T., Csathó, B., 2002. Fusion of LIDAR data and aerial imagery for a more complete surface description, *International Archives of Photogrammetry Remote Sensing and Spatial Information Sciences*, pp. 310-317.
- Shivakumar, S.S., Mohta, K., Pfrommer, B., Kumar, V., Taylor, C.J., 2019. Real time dense depth estimation by fusing stereo with sparse depth measurements, 2019 International Conference on Robotics and Automation (ICRA). IEEE, pp. 6482-6488.
- Tomasi, C., Manduchi, R., Ieee, 1998. Bilateral filtering for gray and color images, Sixth International Conference on Computer Vision, pp. 839-846.
- Veitch-Michaelis, J., Muller, J.P., Storey, J., Walton, D., Foster, M., 2015. DATA FUSION OF LIDAR INTO A REGION GROWING STEREO ALGORITHM, in: Fuse, T., Nakagawa, M. (Eds.), *Indoor-Outdoor Seamless Modelling, Mapping and Navigation*, pp. 107-112.
- Wan, Y., Zhang, Y., Wang, G., Liu, X., 2020. ACCURATE REGISTRATION OF AERIAL IMAGES AND ALS-POINTCLOUD VIA AUTOMATED JUNCTION MATCHING AND PLANAR CONSTRAINTS. *ISPRS Annals of the Photogrammetry, Remote Sensing and Spatial Information Sciences V-2-2020*, 79-86.
- Wang, R., Ferrie, F.P., 2015. Upsampling method for sparse light detection and ranging using coregistered panoramic images. *Journal of Applied Remote Sensing* 9, 095075.
- White, J.C., Wulder, M.A., Vastaranta, M., Coops, N.C., Pitt, D., Woods, M., 2013. The Utility of Image-Based Point Clouds for Forest Inventory: A Comparison with Airborne Laser Scanning. *Forests* 4, 518-536.
- Wujanz, D., Burger, M., Mettenleiter, M., Neitzel, F., 2017. An intensity-based stochastic model for terrestrial laser scanners. *ISPRS Journal of Photogrammetry and Remote Sensing* 125, 146-155.
- Xiao, W., Mills, J., Guidi, G., Rodríguez-Gonzálvez, P., Gonizzi Barsanti, S., González-Aguilera, D., 2018. Geoinformatics for the conservation and promotion of cultural heritage in support of the UN Sustainable Development Goals. *ISPRS Journal of Photogrammetry and Remote Sensing* 142, 389-406.
- Yoon, K.J., Kweon, I.S., 2006. Adaptive support-weight approach for correspondence search. *IEEE transactions on pattern analysis and machine intelligence* 28, 650-656.
- Zabih, R., Woodfill, J., 1994. Non-parametric local transforms for computing visual correspondence, *European Conference on Computer Vision*. Springer Berlin Heidelberg, pp. 151-158.
- Zhang, J., Khoshelham, K., 2020. 3D reconstruction of internal wood decay using photogrammetry and

- sonic tomography. *The Photogrammetric Record* 35, 357-374.
- Zhang, Y., Xiong, X., Zheng, M., Huang, X., 2015. LiDAR Strip Adjustment Using Multifeatures Matched With Aerial Images. *IEEE Transactions on Geoscience and Remote Sensing* 53, 976-987.
- Zhang, Y., Zheng, Z., Luo, Y., Zhang, Y., Wu, J., Peng, Z., 2019. A CNN-Based Subpixel Level DSM Generation Approach via Single Image Super-Resolution. *Photogrammetric Engineering & Remote Sensing* 85, 765-775.
- Zhou, K., Lindenbergh, R., Gorte, B., Zlatanova, S., 2020. LiDAR-guided dense matching for detecting changes and updating of buildings in Airborne LiDAR data. *ISPRS Journal of Photogrammetry and Remote Sensing* 162, 200-213.
- Zhou, Y., Song, Y., Lu, J., 2018. Stereo Image Dense Matching by Integrating Sift and Sgm Algorithm, *International Archives of the Photogrammetry, Remote Sensing and Spatial Information Sciences*, p. 3.
- Zomet, A., Peleg, S., 2002. Multi-sensor super-resolution, *Sixth IEEE Workshop on Applications of Computer Vision, 2002.(WACV 2002). Proceedings. IEEE*, pp. 27-31.